Table of Contents

Chapter 1

Fluoride Salt Cooled High-Temperature Reactor Benchmark

The Fluoride-Salt-Cooled High-Temperature Reactor (FHR) is a reactor concept that uses Tristructural Isotropic (TRISO)-based fuel and a low-pressure liquid fluoride-salt coolant. FHR technology combines FLiBE coolant from Molten Salt Reactor (MSR) technology and TRISO particles from Very-High-Temperature Reactor System (VHTR) technology to enable a reactor with low operating pressure, large thermal margin, and accident-tolerant qualities. To address the technical challenges of Advanced High Temperature Reactor (AHTR) modeling, such as multiple heterogeneity and material cross-section data, the Organisation for Economic Co-operation and Development (OECD)-Nuclear Energy Agency (NEA) and Georgia Institute of Technology (Georgia Tech) initiated the FHR benchmark for the AHTR design in 2019 [1]. The AHTR is a type of FHR that has plate-based fuel in a hexagonal fuel assembly. In section **??**, we gave an overview of the FHR concept, a high-level description of the AHTR design, a review of previous efforts towards modeling these designs, and how these efforts led to the initiation of the benchmark.

The FHR benchmark has several phases, starting with a single fuel assembly simulation without burnup and gradually extending to full core depletion. Table 1.1 outlines the complete and incomplete benchmark phases.

Table 1.1: Phases of the FHR benchmark [1].

Phases	Sub-phases	Description	Completed?
Phase I: Fuel assembly (2D/3D with depletion)	I-A	2D model, steady-state (no depletion)	✓
	I-B	2D model depletion	✓
	I-C	3D model depletion	
Phase II: 3D full core with depletion	II-A	Steady-state (no depletion)	
	II-B	Depletion	
Phase III: 3D full core with feedback & multicycle analysis	III-A	Full core depletion with feedback	
	III-B	Multicycle analysis	

In the subsequent sections, we will describe the benchmark's specifications for the AHTR

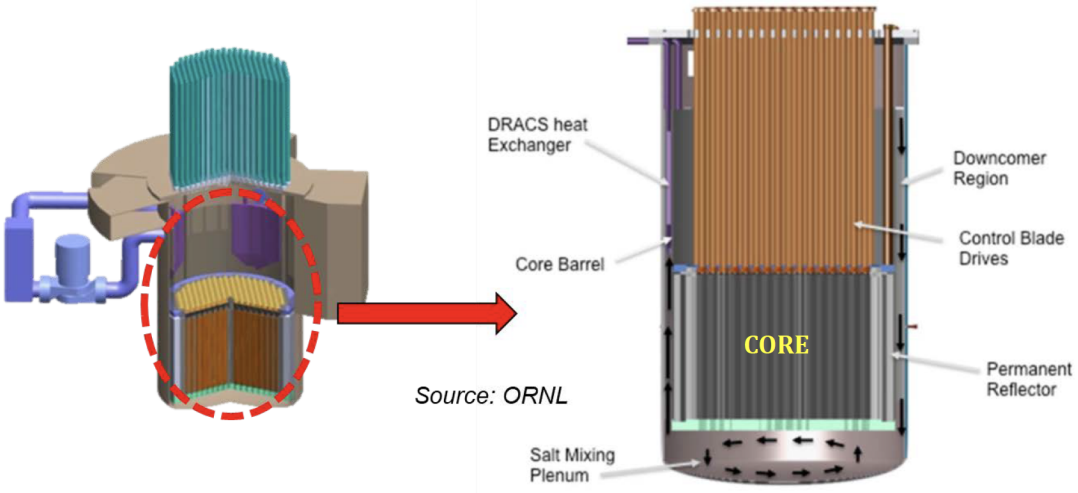

Figure 1.1: Advanced High Temperature Reactor schematic (left) and vessel (right) [1].

design and phase I. Then, we will share our phase I-A and I-B results.

1.1 Benchmark Specifications: AHTR Design

The AHTR has 3400 MWt thermal power and 1400 MW electric power [12]. Figure 1.1 shows the reactor schematic and a vertical cut of the reactor vessel. Figure **??** shows a single fuel assembly's geometry and all assemblies' configuration in the core. A detailed 2D view of the AHTR's hexagonal fuel assembly is shown in Figure 1.2. It features plate-type fuel with hexagonal fuel assembly consisting of eighteen planks arranged in three diamond-shaped sectors, with a central Y-shaped structure and external channel (wrapper). The diamond-shaped sections have 120-deg rotational symmetry with each other [12, 9, 1]. The fuel planks have semi-cylindrical spacers attached, their radius being equal to the coolant channel thickness.

The external channel wrapper and structural Y-shape, as seen in Figure 1.3, are made of C-C composite and have extra notches to hold the fuel plates in place. The gap between the fuel assemblies and fuel plates is filled with Fluoride-Lithium-Beryllium (FLiBe) coolant. The Y-shaped control rod slot at the center of the Y-shape structure contains FLiBe coolant when the control blade is not in the slot [12, 9, 1]. Each fuel plank is made of an isostatically pressed carbon with fuel stripes on each outer side of the plank, as seen in Figure 1.4. The fuel stripes are prismatic

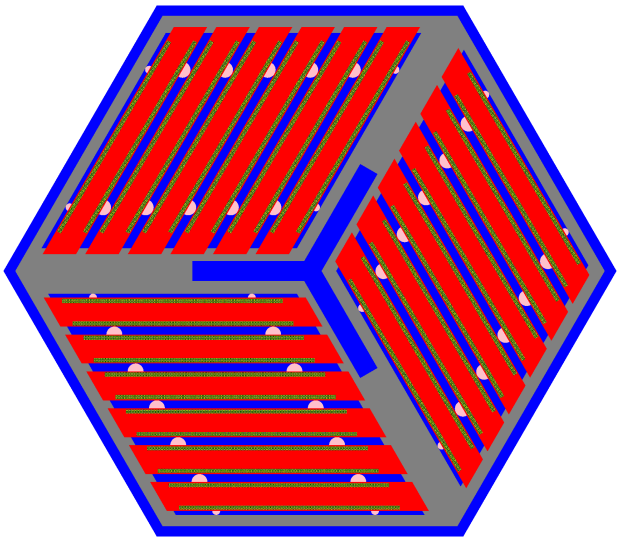

Figure 1.2: Advanced High Temperature Reactor fuel assembly with 18 fuel plates arranged in three diamond-shaped sectors, with a central Y-shaped and external channel graphite structure. Blue: FliBE coolant in between fuel assemblies and plates, and in the control rod slot, Gray: graphite structural components, Red: graphite fuel plank, Pink: graphite spacers, Green: graphite matrix with embedded TRISO particles.

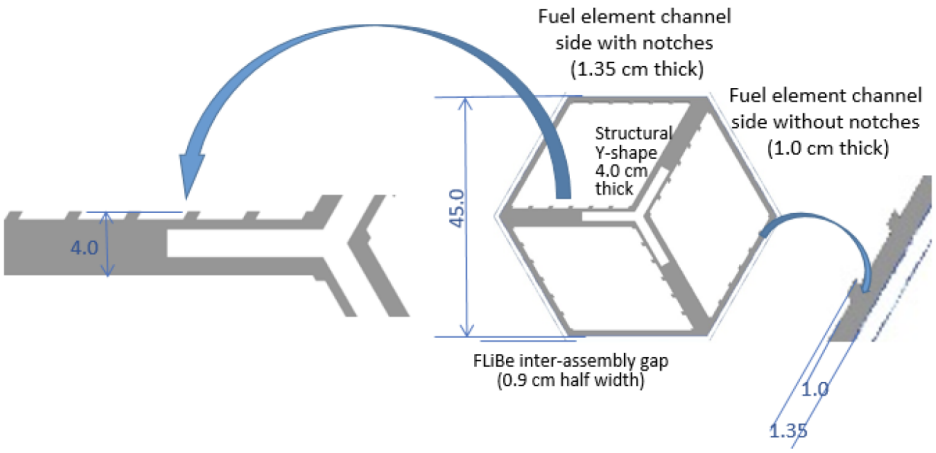

Figure 1.3: Advanced High Temperature Reactor fuel assembly's structural components [1].

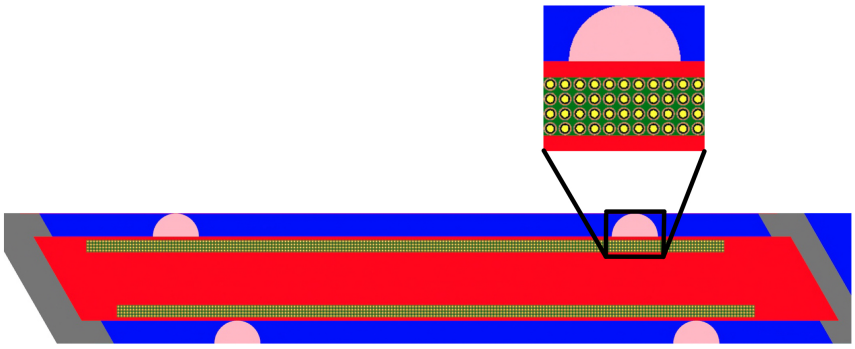

Figure 1.4: Advanced High Temperature Reactor's fuel plank, with the magnification of a spacer and segment of the fuel stripe with embedded TRISO particles.

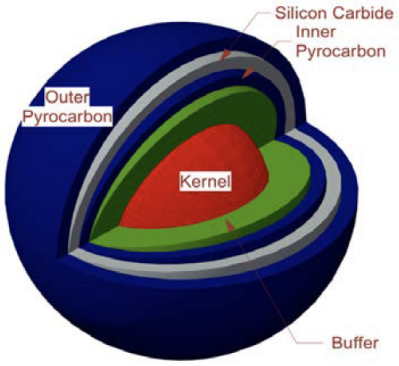

Figure 1.5: Advanced High Temperature Reactor's TRISO particle schematic [1].

regions composed of a graphite matrix filled with a cubic lattice of TRISO particles with a 40% packing fraction. The lattice is 210 TRISO particles wide in the x-direction, four particles deep in the y-direction, and 5936 particles tall in the z-direction. Each TRISO particle has five layers: Oxycarbide fuel kernel, porous carbon buffer, inner pyrolytic carbon, silicon carbide layer, and the outer pyrolitic carbon, as seen in Figure 1.5

Burnable poisons and control rods for reactivity control are also included in some configurations of the AHTR. The burnable poisons consist of europium oxide, Eu_2O_3 and have a discrete or integral (dispersed) option. In the discrete option, small spherical Eu_2O_3 particles are stacked axially at 5 locations in each fuel plank, as shown in Figure 1.6. In the integral option, Eu_2O_3 is homogenously mixed with the fuel plank graphite matrix (including the graphite in fuel stripes matrix and the graphite in the plank ends indented to structural sides, but excluding the graphite in spacers and

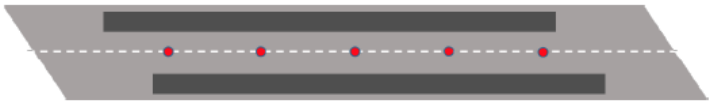

Figure 1.6: Placement of axial stacks of burnable poisons in the Advanced High Temperature Reactor [1].

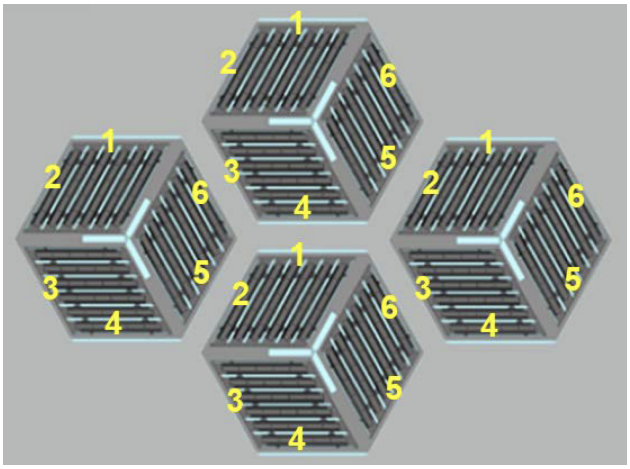

Figure 1.7: Visualization of periodic boundary conditions for a single fuel assembly in the AHTR[1].

graphite in TRISO particles). Each control rod is uniformly composed of Molybdenumhafnium carbide alloy (MHC) and is inserted into the Y-shaped control rod slot and displaces the FLiBe that occupies the slot (Figure 1.2).

1.2 Benchmark Specifications: Phase I

Phase I of the FHR benchmark consists of a steady-state 2D model (phase I-A) and depletion (phase I-B) of one FHR fuel assembly. For a single fuel assembly, the internal 120-degree rotational symmetry is represented by periodic boundary conditions, as seen in Figure 1.7. The benchmark required the following results for phases I-A and I-B:

(a) Effective multiplication factor

(b) Reactivity coefficients (β_{eff}, fuel Doppler coefficient, FLiBe temperature coefficient, graphite temperature coefficient)

(c) Tabulated fission source distribution by 1/5-th fuel stripe

(d) Neutron flux averaged over the whole model tabulated in three coarse energy groups

(e) Neutron flux distribution in three coarse energy groups

(f) Fuel assembly averaged neutron spectrum

Next, we will report the equations we used to calculate the required results listed above.

Reactivity Coefficients (b)

Effective delayed neutron fraction (β_{eff}) is the fraction of delayed neutrons in the core at creation at thermal energies. We assumed 1 energy group and 6 delayed groups for β_{eff}:

$$\beta_{eff} = \sum_k \beta_k \tag{1.1}$$

Reactivity coefficient is the change in reactivity of the material per degree change in the material's temperature. We calculated each reactivity coefficient and its corresponding uncertainty with these equations:

$$\frac{\Delta\rho}{\Delta T} = \frac{\rho_{T_{high}} - \rho_{T_{low}}}{T_{high} - T_{low}} [\frac{pcm}{K}] \tag{1.2}$$

$$\delta\frac{\Delta\rho}{\Delta T} = \frac{\sqrt{\delta(\rho_{T_{high}})^2 + (\delta\rho_{T_{low}})^2}}{T_{high} - T_{low}} [\frac{pcm}{K}] \tag{1.3}$$

Fission Source Distribution / Fission Density (c)

We calculated fission density (FD) with OpenMC's `fission` score (f) for a region divided by the average `fission` score of all the regions:

$$FD_i = \frac{f_i}{f_{ave}} \tag{1.4}$$

where

f_i = Total fission reaction rate [reactions/src]

f_{ave} = average of all f_i [reactions/src]

The uncertainty calculations for f_{ave} and FD_i:

$$\delta f_{ave} = \frac{1}{N}\sqrt{\sum_{i}^{N} f_i^2} \tag{1.5}$$

$$\delta FD_i = |FD_i|\sqrt{(\frac{\delta f_i}{f_i})^2 + (\frac{\delta f_{ave}}{f_{ave}})^2} \tag{1.6}$$

where

$$N = \text{No. of fission score values}$$

Neutron Flux (d, e, f)

OpenMC's `flux` score are in $[\frac{n*cm}{src}]$ units. For the benchmark, we converted flux to $[\frac{n}{cm^2 s}]$ units using the following equations:

$$\Phi_c = \frac{N * \Phi_o}{V} \tag{1.7}$$

$$N = \frac{P * \nu}{Q * k} \tag{1.8}$$

where

Φ_c = Converted Flux $[\frac{neutrons}{cm^2 s}]$

Φ_o = Original Flux $[\frac{neutrons*cm}{src}]$

N = Normalization factor $[\frac{src}{s}]$

V = Volume of fuel assembly $[cm^3]$

P = Power $[\frac{J}{s}]$

$\nu = \frac{\nu_f}{f}$ $[\frac{neutrons}{fission}]$

Q = Energy produced per fission $[\frac{J}{fission}] = 3.2044 * 10^{-11}$ J per U_{235} fission

$k = k_{eff}$ $[\frac{neutrons}{src}]$

Flux standard deviation:

$$\delta\Phi_c = \Phi_c * \sqrt{(\frac{\delta\Phi_o}{\Phi_o})^2 + (\frac{\delta\nu_f}{\nu_f})^2 + (\frac{\delta k}{k})^2 + (\frac{\delta f}{f})^2} \tag{1.9}$$

We calculated reactor power based on the given reference specific power (P_{sp}) of 200 $\frac{W}{gU}$.

$$P = P_{sp} * V_F * \rho_F * \frac{wt\%_U}{100} \tag{1.10}$$

where

$$\begin{aligned}
V_F &= \text{volume of fuel } [cm^3] = \frac{4}{3}\pi r_f^3 * N_{total} \\
r_f &= \text{radius of fuel kernel} \\
N_{total} &= \text{total no. of TRISO particles in fuel assembly} \\
&= 101 * 210 * 4 * 2 * 6 * 3 \\
\rho_F &= \text{density of fuel } [g/cc] \\
wt\%_U &= \frac{at\%_{U235} * AM_{U235} + at\%_{U238} * AM_{U238}}{\sum(at\%_i * AM_i)} * 100 \\
AM &= \text{atomic mass}
\end{aligned}$$

1.2.1 Benchmark Specifications: Phase I-A

For phase I-A, the benchmark specifies that each participant must produce a steady-state 2D model of one fresh fuel assembly for 9 cases and report the required results listed in Section 1.2. Table 1.2 describes each case.

Table 1.2: Description of cases in Phase I-A of the FHR benchmark [1].

Case	Description
1A	Reference case. Hot full power (HFP), with temperatures of 1110K for fuel kernel and 948K for coolant and all other materials (including TRISO particle layers other than fuel kernel). Nominal (cold) dimensions, 9 wt% enrichment, no Burnable Poison (BP), control rods (CRs) out.
2AH	Hot zero power (HZP) with uniform temperature of 948 K, otherwise same as CASE 1A. Comparison with CASE 1A provides HZP-to-HFP power defect.
2AC	Cold zero power (CZP). Same as CASE 2AH, but with uniform temperature of 773 K. Comparison with CASE 2AH provides isothermal temperature coefficient.
3A	CR inserted, otherwise same as CASE 1A.
4A	Discrete europia BP, otherwise same as CASE 1A.
4AR	Discrete europia BP and CR inserted, otherwise same as CASE 1A.
5A	Integral (dispersed) europia BP, otherwise same as CASE 1A.
6A	Increased heavy metal (HM) loading (4 to 8 layers of TRISO) decreased C/HM (from about 400 to about 200) and decreased specific power to 100 W/gU, otherwise same as CASE 1A.
7A	Fuel enrichment 19.75 wt%, otherwise same as CASE 1A.

1.2.2 Benchmark Specifications: Phase I-B

For phase I-B, the benchmark specifies that each participant must produce depletion results for three cases: 1B, 4B, and 7B. These are the same as cases 1A, 4A, and 7A, but with depletion steps added and the critical spectrum assumption. The benchmark assumes that depletion occurs only in the fuel and BPs.

1.3 Results

Several organizations participated in the benchmark with various Monte Carlo and Deterministic neutronics codes, such as Serpent [5], OpenMC [10], and WIMS [6]. We participated in the benchmark with the OpenMC Monte Carlo code [10] and the ENDF/B-VII.1 material library [2]. The `fhr-benchmark` Github repository contains all the results submitted by University of Illinois at Urbana-Champaign (UIUC) for the FHR benchmark [3]. The benchmark used a phased blind approach; thus, participants were asked to submit phase I-A and I-B results without knowledge of other submissions. Petrovic et al. [8] describes the preliminary results of the benchmark results across several institutions and concludes that the overall observed agreement is satisfactory. In the subsequent sections, we will share the results obtained by UIUC.

1.3.1 Results: Phase I-A

Petrovic et al. [8] compared the effective multiplication factor for all participants and phase I-A cases in the FHR benchmark. They reported that the standard deviation between participants for each case was in the 231 to 514 pcm range, acceptable and notably close given a blind benchmark, assuring us that our phase I-A results are acceptable and in agreement with other benchmark participants. Next, we will present our results for phase I-A and describe and explain the observed trends.

Table 1.2 reports phase I-A results for effective multiplication factor and reactivity coefficients. We ran the simulations on UIUC's BlueWaters supercomputer [7] with 64 XE nodes, which each have 32 cores. To reduce the statistical uncertainty of keff to ~10pcm, we ran each simulation with 500 active cycles, 100 inactive cycles, and 200000 neutrons. Each simulation took wall-clock-time (WCT) ranging from 2 to 5 hours.

Table 1.3: FHR Benchmark UIUC's phase I-A results [3].

Case	**Summary**	**WCT [hr]**	k_{eff}	β_{eff}*	**Fuel** $\frac{\Delta\rho}{\Delta T}$	**FliBe** $\frac{\Delta\rho}{\Delta T}$	**Graphite** $\frac{\Delta\rho}{\Delta T}$
1A	Reference	2.82	1.39389±0.00010	0.006534	-2.24±0.15	-0.15±0.15	-0.68±0.15
2AH	HZP	2.82	1.40395±0.00010	0.006534	-3.14±0.15	-0.20±0.14	-0.85±0.14
2AC	CZP	2.75	1.41891±0.00010	0.006534	-3.36±0.14	-0.11±0.14	0.07±0.14
3A	CR	2.49	1.03147±0.00011	0.006534	-4.03±0.28	-0.83±0.27	-3.18±0.29
4A	Discrete BP	5.08	1.09766±0.00010	0.006542	-4.06±0.24	-1.55±0.23	-6.51±0.24
4AR	Discrete BP + CR	4.59	0.84158±0.00010	0.006553	-5.60±0.49	-1.78±0.46	-10.44±0.47
5A	Dispersed BP	2.33	0.79837±0.00009	0.006556	-5.09±0.40	-4.87±0.40	-22.99±0.38
6A	Increased HM	3.52	1.26294±0.00011	0.006556	-4.46±0.19	0.16±0.20	-0.39±0.20
7A	19.75% Enriched	2.21	1.50526±0.00010	0.006530	-2.49±0.13	-0.12±0.12	-0.62±0.12

* All β_{eff} values have an uncertainty of 0.000001.

Cases 2AH and 2AC are at zero power, meaning that the fuel assembly is exactly critical but not producing any energy. For both cases, keff is higher than the reference case 1A, which we attribute to lower fuel temperatures; at higher fuel temperatures, doppler broadening occurs, resulting in more neutron capture, thus, lowering keff. As expected, keff is lower for cases 3A, 4AR, and 5A than reference case 1A since those cases introduced burnable poisons and control rods to the fuel assembly. Also, as expected, keff is higher for case 7A than reference case 1A since it has a higher enrichment. However, case 6A deviated from expectations with a lower keff despite an increase in HM loading. This behavior is due to reduced moderation and worsened fuel utilization

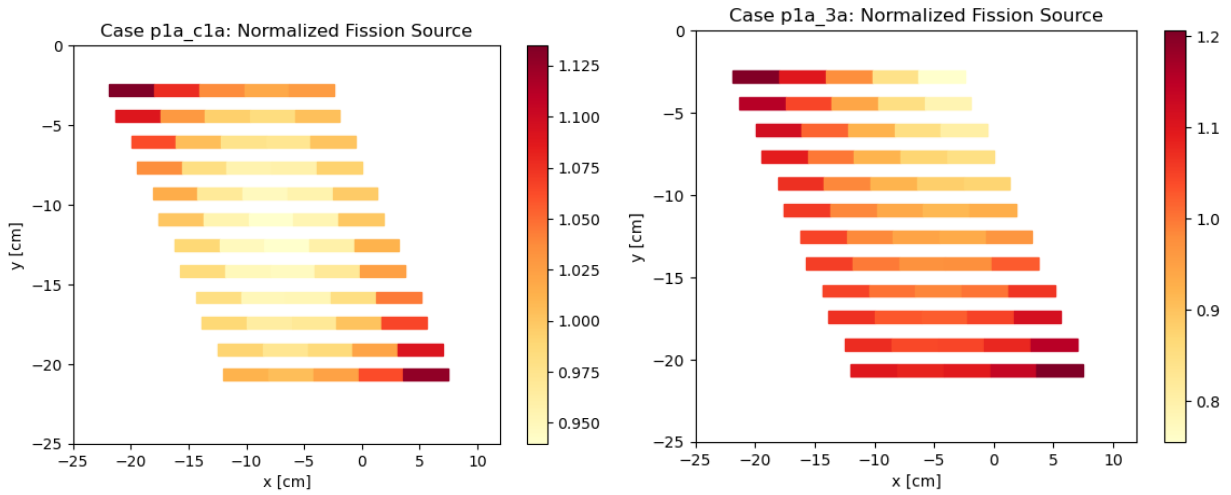

Figure 1.8: Fission Source Distribution per $1/5^{th}$ fuel stripe for FHR Benchmark's phase I-A Case 1A (left) and Case 3A (right).

brought about by self-shielding, demonstrating an increase in fuel packing fraction does not always correspond with an increased keff.

β_{eff} increased by 10-20pcm for cases 4A, 4AR, 5A, and 6A, compared to reference case 1A, due to the introduction of control rods and poisons, which shifts the average neutron velocity to higher values resulting in decreased thermal fission and increased fast fission[11]. Table 1.3 reports that most of the temperature coefficients are negative, exemplifying the AHTR's passive safety behavior. Negative reactivity feedback results in a self-regulating reactor; if the reactor's power rises, resulting in temperature increase, the negative reactivity will, in turn, reduce power.

Figure 1.8 shows the fission source distribution by $1/5^{th}$ fuel stripe for cases 1A and 3A. Case 4AR has a similar fission source distribution as case 3A since both cases have control rod insertion. All other cases have similar fission source distributions to case 1A. For case 1A, intuitively, we would assume that the highest fission source would occur in the center of the diamond fuel segment; however, the opposite is true. Power peaking occurs on exterior stripes and is minimum on the interior stripes. Gentry et al. [4] reported similar power peaking phenomena towards the lattice cell's exterior closest to the Y-shaped carbon support structure where the thermal flux is most elevated. The lowest power is found in the interiors of the lattice tri-sections. This fission source distribution is caused by diminished resonance escape probability in the interior due to the higher relative fuel-to-carbon volume ratio. This diminished fission source in the interior stripes

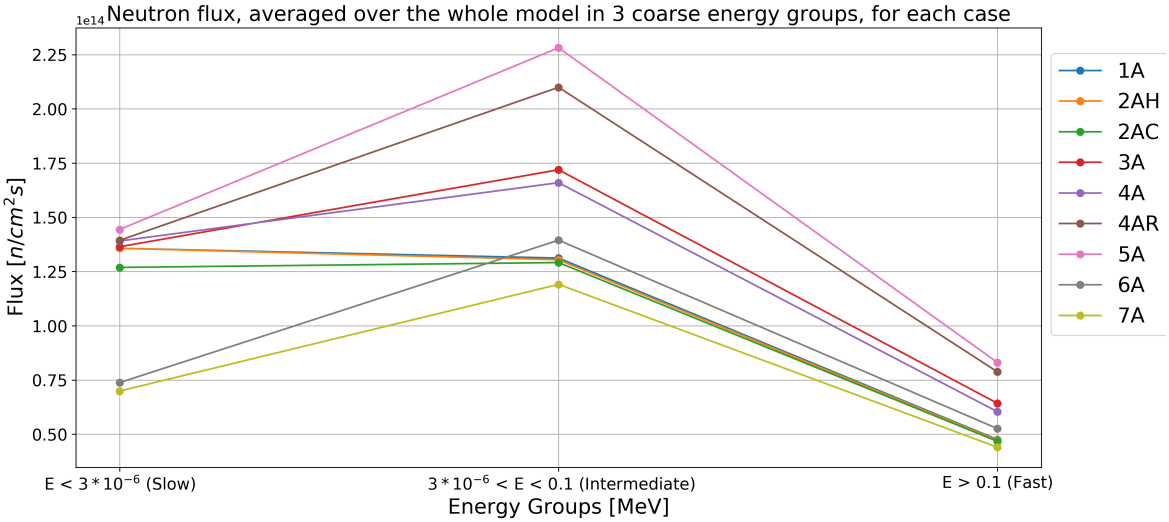

Figure 1.9: Neutron Flux, averaged over the whole model, tabulated in three coarse energy groups for each phase I-A case.

phenomena is exaggerated in cases 6A and 7A since there is a higher fuel-to-carbon ratio. For case 3A with an inserted control rod, the fission source is lower in the $1/5^{th}$ stripes closer to the control rod.

Figure 1.9 shows the average neutron flux in the fuel assembly in three coarse energy groups. Most of the cases have the most flux in the intermediate group, followed by the thermal group, and the least flux in the fast group. Figure 1.10 shows the neutron flux distribution for case 1A, 3A, and 6A for three coarse energy groups. For all three cases, fast-flux peaks in the diamond-shaped sectors containing the fuel stripes, whereas thermal flux peaks outside of the diamond-shaped sectors; this is attributed to fission occurring at thermal energies in the fuel stripe area. For case 3A, the thermal and intermediate neutron flux is depressed in the fuel assembly's control rod region. Case 6A has increased HM; thus, we see that fast-flux peaking and the thermal flux dip in the fuel stripe area is more pronounced than case 1A. Figure 1.11 shows the neutron spectrum for cases 1A and 6A. Case 7A has a similar neutron spectrum as case 6A since both cases have higher fuel content. All other cases have a similar neutron spectrum to case 1A. The neutron spectrum is faster for case 6a and case 7a due to more heavy metal loading and higher enrichment.

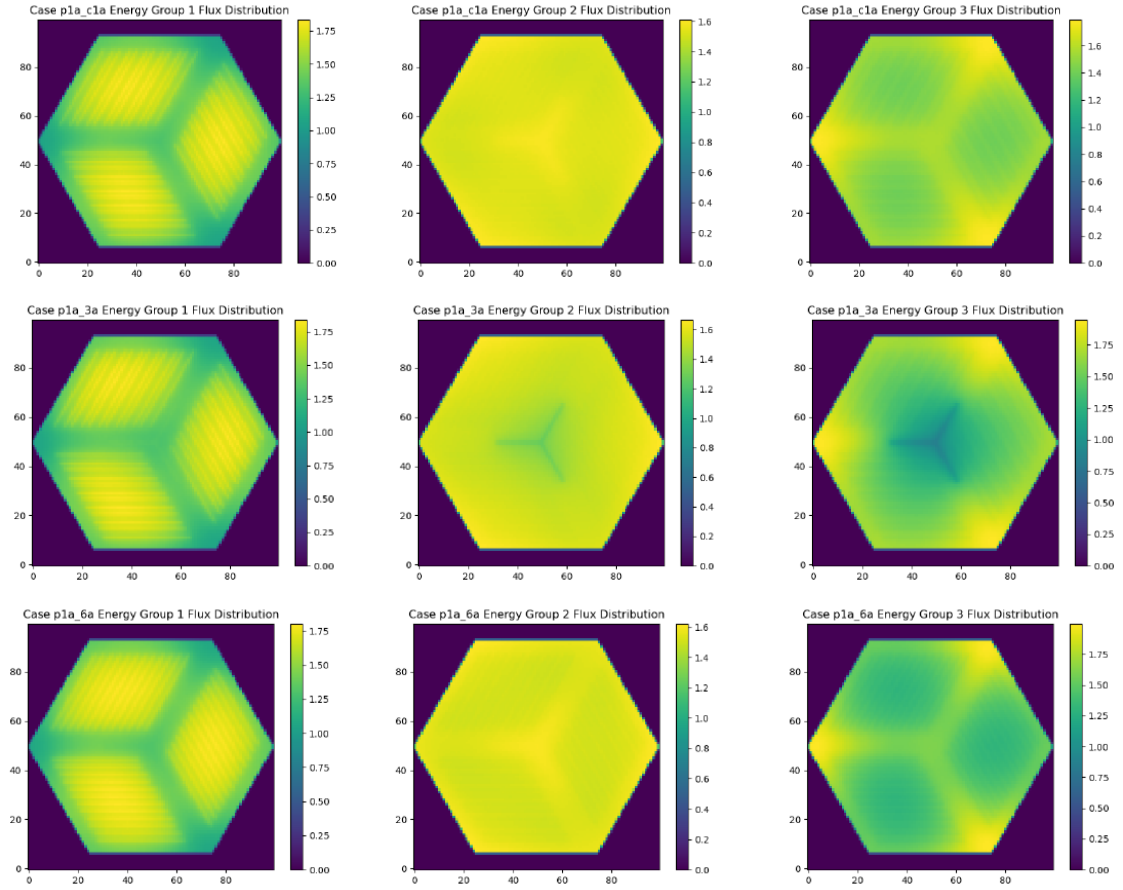

Figure 1.10: Neutron Flux distribution in 100 by 100 mesh for three coarse energy groups: case 1A (above), case 3A (middle), case 6A (below)

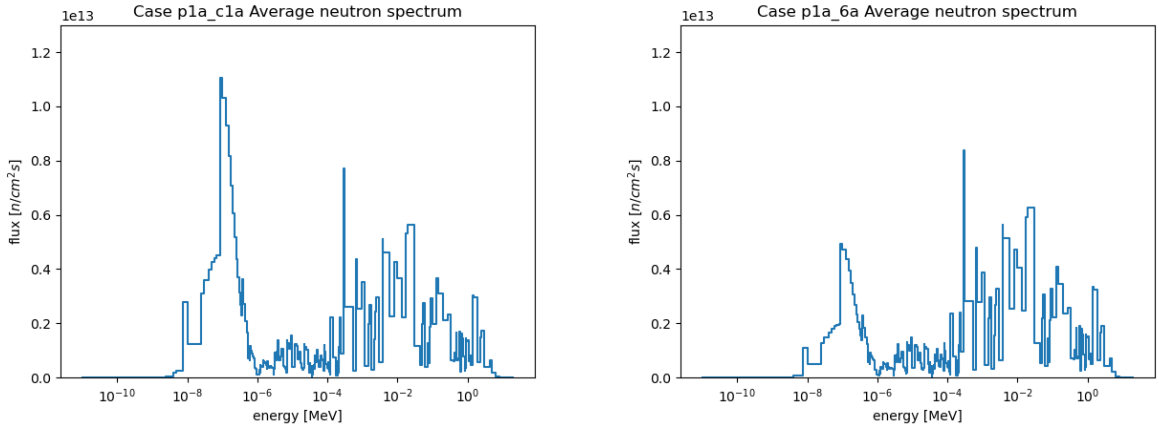

Figure 1.11: Neutron Spectrum for FHR Benchmark's phase I-A Case 1A (left) and Case 6A (right).

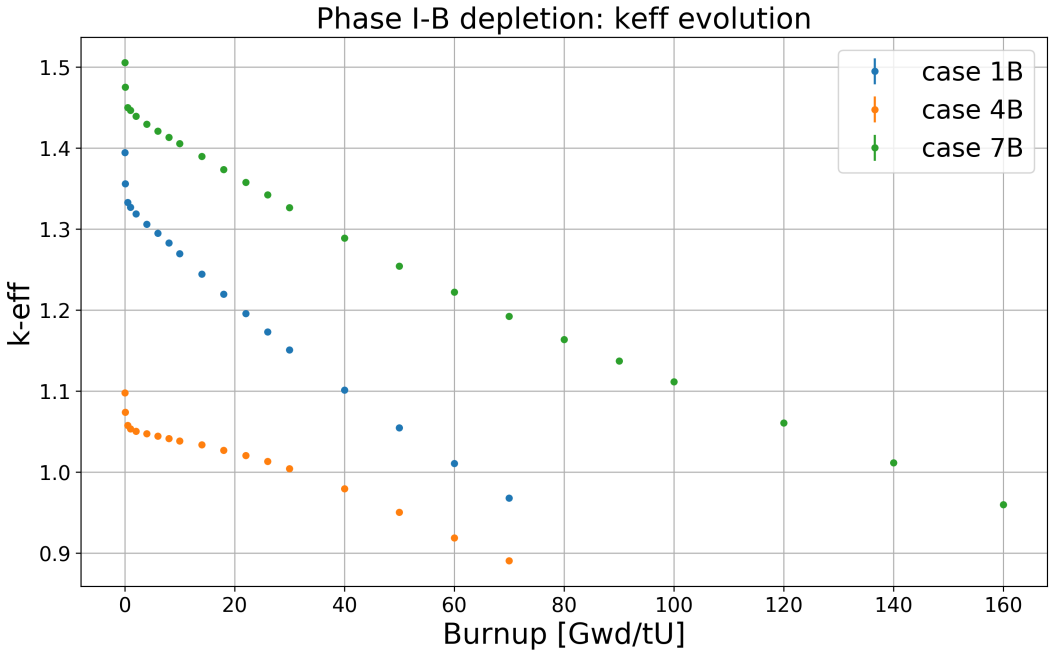

Figure 1.12: FHR Benchmark UIUC's phase I-B depletion k-eff evolution for cases 1B, 4B, and 7B. Case 1B is the reference case, case 4B is the discrete BP case, and case 7B is the 19.75% enrichment case. Error bars are included but are barely visible due to the low uncertainty of ~40pcm.

1.3.2 Results: Phase I-B

Figure 1.12 shows the evolution of effective multiplication factor during depletion for cases 1B, 4B, and 7B. The effective multiplication factor at 0 burnup corresponds to each case's corresponding phase I-A k-eff value reported in Table 1.3. Case 1B is the reference case with 9% fuel enrichment and no BPs. Case 1B's k-eff steadily decreases until it reaches 0.967845 at the final 70 GWd/tU burnup. Case 4B includes burnable poisons resulting in a lower initial k-eff. Its k-eff decreases at a slower rate in the beginning due to the presence of burnable poisons, which decreases flux in the core. At approximately 20 GWd/tU, k-eff begins decreasing at a faster rate, assumedly due to burn-up of the poison material. Case 7B has a 19.75% fuel enrichment, resulting in a higher initial k-eff. With a higher enrichment, the fuel can achieve a burnup of 160 GWd/tU.

1.4 Summary

This chapter described the FHR benchmark specifications, AHTR design, and the phase I-A and I-B results obtained by the UIUC team. The benchmark results highlight the AHTR's passive safety behavior with negative temperature coefficients. Results such as a lower keff for the AHTR configuration with higher HM loading gave insight into how increased fuel packing does not always correspond with increased keff due to self-shielding effects. These results hint at the possibility of minimizing fuel required by optimizing for inhomogeneous fuel distributions within the core. This will be further explored in the next chapters.

References

[1] Fluoride Salt-Cooled High-Temperature Reactor (FHR) Benchmark. URL: https://www.oecd-nea.org/jcms/pl_20249/fluoride-salt-cooled-high-temperature-reactor-fhr-benchmark.

[2] M. B. Chadwick, M. Herman, P. Obloinsk, M. E. Dunn, Y. Danon, A. C. Kahler, D. L. Smith, B. Pritychenko, G. Arbanas, R. Arcilla, R. Brewer, D. A. Brown, R. Capote, A. D. Carlson, Y. S. Cho, H. Derrien, K. Guber, G. M. Hale, S. Hoblit, S. Holloway, T. D. Johnson, T. Kawano, B. C. Kiedrowski, H. Kim, S. Kunieda, N. M. Larson, L. Leal, J. P. Lestone, R. C. Little, E. A. McCutchan, R. E. MacFarlane, M. MacInnes, C. M. Mattoon, R. D. McKnight, S. F. Mughabghab, G. P. A. Nobre, G. Palmiotti, A. Palumbo, M. T. Pigni, V. G. Pronyaev, R. O. Sayer, A. A. Sonzogni, N. C. Summers, P. Talou, I. J. Thompson, A. Trkov, R. L. Vogt, S. C. van der Marck, A. Wallner, M. C. White, D. Wiarda, and P. G. Young. ENDF/B-VII.1 Nuclear Data for Science and Technology: Cross Sections, Covariances, Fission Product Yields and Decay Data. *Nuclear Data Sheets*, 112(12):2887–2996, December 2011. doi:10.1016/j.nds.2011.11.002.

[3] Gwendolyn Chee. arfc/fhr-benchmark, 2021.

[4] Cole Andrew Gentry. *Development of a Reactor Physics Analysis Procedure for the Plank-Based and Liquid Salt-Cooled Advanced High Temperature Reactor*. PhD thesis, 2016.

[5] Jaakko Leppanen, Maria Pusa, Tuomas Viitanen, Ville Valtavirta, and Toni Kaltiaisenaho. The Serpent Monte Carlo code: Status, development and applications in 2013. *Annals of Nuclear Energy*, 82:142–150, August 2014. doi:10.1016/j.anucene.2014.08.024.

[6] B. A. Lindley, J. G. Hosking, P. J. Smith, D. J. Powney, B. S. Tollit, T. D. Newton, R. Perry, T. C. Ware, and P. N. Smith. Current status of the reactor physics code WIMS and recent developments. *Annals of Nuclear Energy*, 102:148–157, 2017. ISBN: 0306-4549 Publisher: Elsevier.

[7] NCSA. About Blue Waters: The National Center for Supercomputing Applications at the University of Illinois at Urbana-Champaign, 2017. http://www.ncsa.illinois.edu/. URL: http://www.ncsa.illinois.edu/.

[8] Bojan Petrovic, Kyle M. Ramey, Ian Hill, E. Losa, M. Elsawi, Z. Wu, C. Lu, J. Gonzalez, D. Novog, G. Chee, K. D. Huff, M. Margulis, N. Read, and Eugene Shwageraus. Preliminary results for the NEA FHR benchmark phase I-A and I-B (submitted). In *ANS M&C 2021 - The International Conference on Mathematics and Computational Methods Applied to Nuclear Science and Engineering*, Raleigh, North Carolina, 2021. ANS.

[9] Kyle M. Ramey and Bojan Petrovic. Monte Carlo modeling and simulations of AHTR fuel assembly to support V&V of FHR core physics methods. *Annals of Nuclear Energy*, 118:272–282, August 2018. URL: https://linkinghub.elsevier.com/retrieve/pii/S0306454918301816, doi:10.1016/j.anucene.2018.04.003.

[10] Paul K. Romano and Benoit Forget. The OpenMC Monte Carlo particle transport code. *Annals of Nuclear Energy*, 51:274–281, January 2013. URL: http://www.sciencedirect.com/science/article/pii/S0306454912003283, doi:10.1016/j.anucene.2012.06.040.

[11] Mina Torabi, A. Lashkari, Seyed Farhad Masoudi, and Somayeh Bagheri. Neutronic analysis of control rod effect on safety parameters in Tehran Research Reactor. *Nuclear Engineering and Technology*, 50(7):1017–1023, 2018. ISBN: 1738-5733 Publisher: Elsevier.

[12] Venugopal Koikal Varma, David Eugene Holcomb, Fred J. Peretz, Eric Craig Bradley, Dan Ilas, A. L. Qualls, and Nathaniel M. Zaharia. AHTR mechanical, structural, and neutronic preconceptual design. Technical report, Oak Ridge National Lab.(ORNL), Oak Ridge, TN (United States), 2012.